IEEE Photonics Journal
An IEEE Photonics Society Publication

Open Access

Power-Efficiency Enhanced Thermally Tunable Bragg Grating for Silica-on-Silicon Photonics

Volume 7, Number 2, April 2015

P. A. Cooper
L. G. Carpenter
C. Holmes
C. Sima
J. C. Gates
P. G. R. Smith

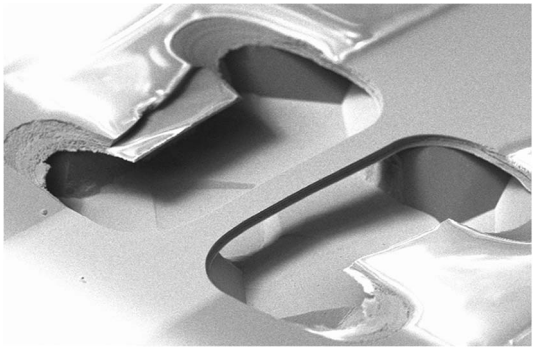

DOI: 10.1109/JPHOT.2015.2415673
1943-0655

IEEE photonics SOCIETY

IEEE

Power-Efficiency Enhanced Thermally Tunable Bragg Grating for Silica-on-Silicon Photonics

P. A. Cooper,[1] L. G. Carpenter,[1] C. Holmes,[1] C. Sima,[2] J. C. Gates,[1] and P. G. R. Smith[1]

[1]Optoelectronics Research Centre, University of Southampton, Highfield Campus, Southampton, SO17 1BJ, U.K.
[2]Next Generation Internet Access National Engineering Laboratory, Huazhong University of Science and Technology, Wuhan 430074, China

DOI: 10.1109/JPHOT.2015.2415673

Manuscript received February 3, 2015; revised March 12, 2015; accepted March 14, 2015. Date of current version April 3, 2015. This work was supported by the Engineering and Physical Sciences Research Council under Grant EP/I003835/1. Corresponding author: P. A. Cooper (e-mail: pac1g11@soton.ac.uk).

Abstract: A thermally tunable Bragg grating device has been fabricated in a silica-on-silicon integrated optical chip, incorporating a suspended microbeam improving power efficiency. A waveguide and Bragg grating are defined through the middle of the microbeam via direct ultraviolet writing. A tuning range of 0.4 nm (50 GHz) is demonstrated at the telecommunication wavelength of 1550 nm. Power consumption during wavelength tuning is measured at 45 pm/mW, which is a factor of 90 better than reported values for similar bulk thermally tuned silica-on-silicon planar devices. The response time to a step change in heating is longer by a similar factor, as expected for a highly power-efficient device. The fabrication procedure involves a deep micromilling process, as well as wet etching and metal deposition. With this response, the device would be suitable for trimming applications and wherever low modulation frequencies are acceptable. A four-point-probe-based temperature measurement was also done to ascertain the temperature reached during tuning and found an average volume temperature of 48 °C, corresponding to 0.4 nm of tuning. The role of stress-induced buckling in device fabrication is included.

Index Terms: Bragg grating, thermal tuning, microbeam, power efficiency.

1. Introduction

Microbeams are a common structure in Micro-Opto-Electro-Mechanical (MOEM) devices. In their most basic form they consist of a beam clamped at both ends suspended over a substrate. A variety of applications that take advantage of the special properties of microbeams can be found in the literature; Guckel *et al.* [1] fabricated microbeams to measure the stress in a deposited polysilicon film. A thermally driven microvalve was fabricated by Lisec *et al.* [2]. Joe *et al.* used the resonant frequency behavior of microbeams for gas-sensing applications [3]. Optical applications include a bridge suspended thermo-optic phase shifter [4] in silica-on-silicon and a tunable Bragg grating in a silicon waveguide [5].

Bragg gratings in silica waveguides have already been proven in fields such as telecoms, sensing, and quantum information experiments [6]. The ability to control either the reflected wavelength or the spectral shape of the Bragg grating can lead to new types of devices.

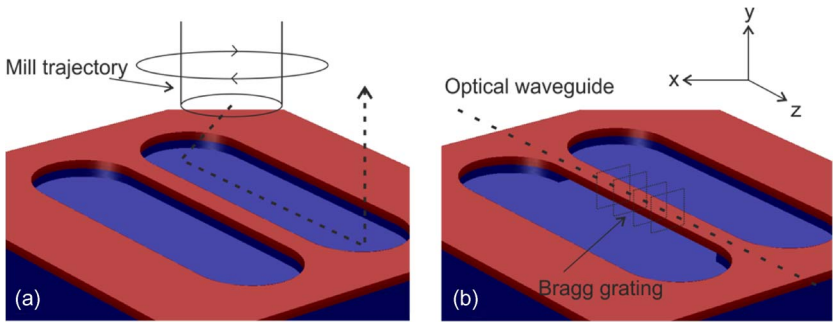

Fig. 1. (a) Structure geometry following milling. The glass layers are shown in red, while the silicon is blue. The trajectory of the milling cutter is shown. (b) Structure after KOH wet etching showing how the silicon underneath the microbeam has been removed. The locations of the optical waveguide and Bragg grating are also shown with dotted lines. For simplicity, the "run-up" section described later is not included in this schematic diagram.

Wavelength tuning can be used in add/drop multiplexers for Dense Wavelength Division Multiplexing (DWDM) [7]. Tuning the chirp or non-linearity of a grating has applications in active dispersion control for communications systems [8].

The approach of undercutting a laser written microstructure has been used previously to demonstrate microcantilevers, clamped only at a single end [9], and membranes [10]. This new device allows for transmission operation and simplifies the placement of the heating element.

The microbeam geometry is expected to give enhanced thermal tuning efficiency performance due to its thermal isolation from the environment and the extremely low heat capacity of the microbeam. As the silicon substrate is an excellent conductor of heat, it efficiently sinks heat away from the waveguide, thereby increasing the thermal load and decreasing the energy efficiency when tuning in a bulk substrate. In a microbeam device the air gap around the microbeam provides effective thermal isolation. The current interest in fabricating optical waveguide chips for quantum information processing requires large numbers of heating elements for optical phase tuning, resulting in the chip having to dissipate large amounts of power to remain at stable temperature [11]. Incorporating microbeam structures at heating points could drastically reduce the amount of bulk heating and cross-talk between phase shifters.

Various methods of optical tuning have been reported in the literature for integrated planar devices; piezoelectric actuation was used in a phase shifting device by Donati *et al.* [12] and liquid crystal tuning was demonstrated by Adikan *et al.* [13]. The ideal method of tuning will depend on different factors including device format, tuning range required and response time. Thermal tuning is a proven method of tuning for integrated optics and was selected for this work due to the reliability and relative simplicity of fabrication.

2. Thermal Tuning Theory

In our device, we thermo-optically tune a Bragg grating, located in a microbeam, and demonstrate control of the optical path length of a Fabry–Pérot cavity defined across the microbeam. The graphic in Fig. 1. shows how the structure of the microbeam is created through a combination of micromilling and wet etching as well as the location of the optical elements in relation to the physical structure.

A Bragg grating is a region of periodically modulated refractive index that reflects light resonantly at wavelengths given by the Bragg condition. The Bragg condition gives the center wavelength λ_B reflected by a Bragg grating and is given by

$$\lambda_B = 2n_{eff}\Lambda \tag{1}$$

where Λ is the pitch of the Bragg grating, and n_{eff} is the effective refractive index of the waveguide mode. A simple mathematical model can be developed to model the efficiency of thermal tuning by considering how the variables in (1) are affected by temperature and the associated

changes in the waveguide. Thermal tuning can change the Bragg condition in three ways: first, via thermo-optic effect; second, through stress-optic; and third, by grating pitch expansion, which in our device is modified due to the mechanical anchoring at either end of the beam. The shift in Bragg peak wavelength can be expressed by the change in refractive index with

$$\Delta\lambda_B = \frac{\Delta n}{n_{eff}}\lambda. \tag{2}$$

First, due to the thermo-optic effect in most materials, n is a function of temperature. For small temperature changes the relationship is linear and is given by

$$\Delta n = \xi \Delta T. \tag{3}$$

Here, ξ is the thermo-optic coefficient and has a value of 1×10^{-5} K^{-1} for pure silica glass [14].

For our device, we know that the modal refractive index $n_{eff} = 1.448$ for wavelengths around 1550 nm. By combining (2) and (3), the theoretical tuning sensitivity of the device due to the thermo-optic effect is 10.7 pm/°C, and this is consistent with the values of standard non-MEM's type devices [15].

Second, the stress-optic effect, also referred to as photoelasticity, describes the effect of stress on the refractive index. In a constrained system heating will lead to thermal stress developing as the material is not free to expand. As stress is a tensor it is necessary to consider the change in refractive index along three orthogonal axis. The three components of refractive index are given by

$$n_x = n - pS_x - q(S_y + S_z) \tag{4}$$
$$n_y = n - pS_y - q(S_x + S_z) \tag{5}$$
$$n_z = n - pS_z - q(S_x + S_y) \tag{6}$$

where S_x, S_y, and S_z are the normal components of the stress tensor and the stress optic coefficients $p = 6.5 \times 10^{-13}$ Pa^{-1} and $q = 4.2 \times 10^{-12}$ Pa^{-1} for pure silica glass [16]. The coordinate system used is as shown in Fig. 1. If a normal stress is applied along the microbeam axis, this causes stresses in the orthogonal directions with a magnitude determined by Poisson's ratio

$$S_x = -\nu S_z \tag{7}$$
$$S_y = -\nu S_z. \tag{8}$$

Here ν is Poisson's ratio with a value of 0.17 for silica glass [17]. When (7) and (8) are substituted into (4), the refractive index change as a function of S_z is obtained as

$$\Delta n_{x,y} = S_z(p\nu - q(1-\nu)). \tag{9}$$

If the stress is caused by constrained thermal expansion it will be proportional to the temperature change as

$$S_z = E\alpha\Delta T. \tag{10}$$

Here, E is the Young's modulus of silica, taken to be 73.1 GPa. α is the coefficient of thermal expansion which was taken to be 0.55×10^{-7} [17]. This results in a negative tuning sensitivity due to the stress-optic effect of -0.12 pm/°C. This simple analysis is not capable of distinguishing any potential birefringence caused by the stress-optic effect.

Thirdly, in addition to the stress induced by thermal changes, the microbeam will also tend to expand, altering the period of the grating. In an unconstrained system, thermal expansion will cause an increase in the pitch of the Bragg grating

$$\Delta\Lambda = \alpha\Delta T\Lambda. \tag{11}$$

$\Delta\Lambda$ is the increase in pitch of the Bragg grating. For the device described the thermo-optic effect will always be contributing during the tuning. A further complication is that a stressed

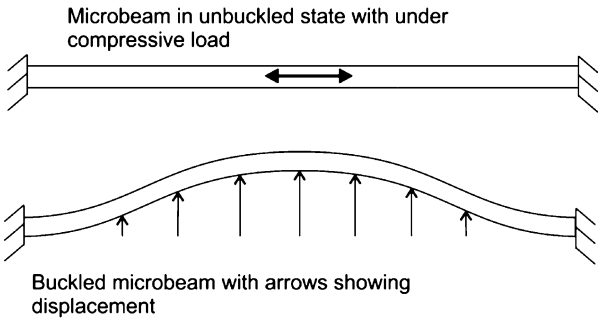

Fig. 2. Graphic showing how a microbeam will eventually buckle to relieve compressive stress when mechanically anchored at both ends.

beam can undergo buckling to release stress which will affect how subsequent strains develop. If a microbeam is in the buckled state thermal strain will be only partially constrained and some grating pitch expansion will occur. If it is unbuckled, thermal stresses will occur, but the grating pitch will not change appreciably.

As mentioned, it is possible for an axially stressed beam to undergo buckling if its length exceeds a critical length. Buckling is a sudden, discontinuous change of beam shape in a response to a critical applied axial load in a beam. In a symmetric beam with uniform load there is a bifurcation and buckling in any direction is possible. However if the beam has shape imperfections or cross-sectionally varying stresses these may help to define the preferred buckling direction. A slightly bent beam under increasing stress will deflect continuously however it will not buckle until the critical load level is reached. The buckled beam has a characteristic shape known as the buckled mode and will generally have its maximum displacement at the center of the beam. The stress, S, required to cause buckling in a beam with length L_c is given by the Euler-Bernoulli equation [18]

$$S = \frac{\pi^2 E h^2}{3L_c^2}. \tag{12}$$

L_c is the critical length of the microbeam beyond which buckling occurs. h is the thickness of beam. Fig. 2 illustrates how an initially straight microbeam buckles to a lower energy configuration with the characteristic shape of the first buckling mode.

3. Fabrication

The fabrication process for our tunable Bragg grating device includes physical micromachining, wet etching and metal deposition. The initial substrate consists of two layers of Flame Hydrolysis Deposition glass on a silicon wafer with a 15 μm thermally grown layer to act as an underclad. The core layer is doped with germanium to increase photosensitivity. The wafer is diced with a commercial dicing saw to produce device sized chips or die. In this work microbeams of two lengths were fabricated. A 1 mm long microbeam contained optical elements and was characterized both optically and mechanically, whilst a 1.5 mm-microbeam was characterized mechanically.

For the wet etch to fully undercut the microbeam, two deep trenches must be machined through the silica exposing the silicon. The grooves must be sufficiently deep to prevent premature formation of slow etching $\langle 100 \rangle$ etch planes, which drastically reduce the etch rate. Reactive ion etching (RIE) and inductively coupled etching (ICP) would have required very long process times to reach this depth of groove. For this reason physical micromachining was selected as the machining time was shorter and fabrication of lithographic masks was not required, and in addition is capable of yielding very smooth surfaces [19]. A micro-mill was used to fabricate two grooves to a depth of 80 μm. The micro-mill has a Loadpoint Bearings air-bearing spindle with dynamic runout better than 1 μm. The workpiece is translated on an air-bearing

TABLE 1

Machining parameters used for micromilling of grooves

Tool diameter	0.5 mm
Mill type	UKAM 500 μm diameter diamond microdrill
Spindle speed	60,000 rpm
Linear feed rate	0.1 mm/min

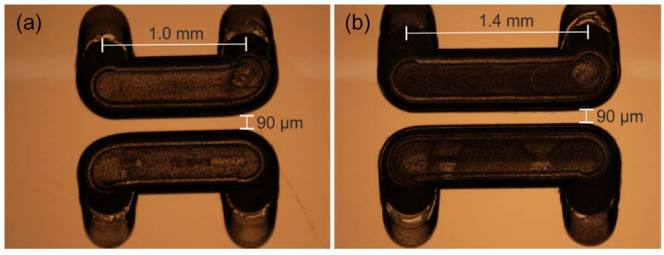

Fig. 3. Optical microscope images of milled grooves prior to UV writing and etching. (a) 1 mm. (b) 1.5 mm.

Aerotech X,Y translation stage with nanometer level resolution. Table 1 shows the processing parameters used during the milling operation.

It was essential to minimize edge chipping and cracks in the silica as these could cause failure of the microbeam at the etch stage. Fig. 3 shows two milled grooves after optimization and demonstrates that the edge chipping has been kept to a low level.

During development of the milling process it was found that top edge chipping occurred more frequently at the start and end of grooves where the tool was either engaging or disengaging the surface. For this reason, "run-up" sections at 90° to the main grooves were introduced and can be seen in Fig. 3. These kept initial edge chipping out the way without affecting the function of the device. Each "run-up" was 0.5 mm in length and the tool took a linear descent to the cut-depth of 80 microns.

The chip is loaded under high-pressure hydrogen to allow diffusion into the core, increasing photosensitivity. Single mode waveguides and Bragg gratings are written into the glass layer using the direct UV writing process [20]. Fig. 4 shows the layout of the optical elements in the device. A Gaussian apodized Bragg grating with central reflection wavelength of 1565 nm is located in the microbeam whilst two Bragg gratings with a peak reflection wavelength of 1550 nm are written either side to form a Fabry–Pérot cavity. As the Fabry–Pérot cavity is formed with two Gaussian apodized Bragg gratings, spectrally it consists of sharp fringes with periodicity determined by the cavity length with a Gaussian function envelope. The cavity was used to determine the response time of the microbeam to applied heating due to sensitivity of fringe position to changes in the optical path length.

A potassium hydroxide wet etch was used to remove the exposed silicon releasing the microbeam. The chip was immersed in 4.5 mol/l solution at 75 °C for 5 hours. Fig. 5 shows microscope images of the released microbeams. The glass microbeam is almost transparent but can be seen above the silicon floor in the microscope image. The irregular silicon etch features are a result of anisotropic etching of the groove bases due to the crystalline planes of the ⟨100⟩ substrate.

The reflection spectrum of the device was characterized optically before and after etching. Fig. 6 shows a comparison of the spectra before and after etching. The Bragg grating in the microbeam is shown at around 1566 nm whilst the Fabry–Pérot cavity peak location is at approximately 1552 nm. A zoomed-in section of the spectra is plotted to show the Fabry–Pérot fringes more clearly.

A gold heating strip is deposited using evaporative deposition. A 5 nm seed layer of chromium is first deposited to improve adhesion between the gold and silica glass. Polyimide tape was

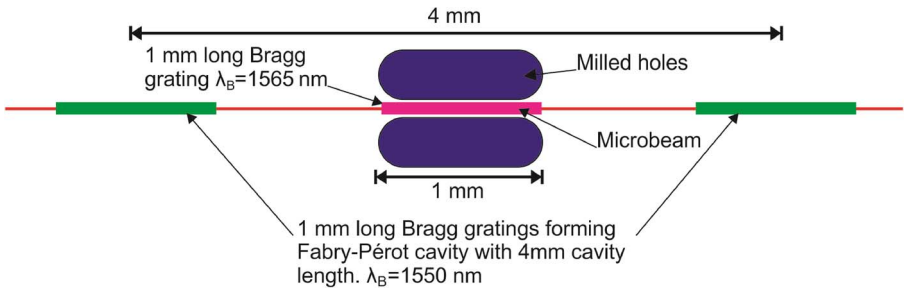

Fig. 4. Schematic showing layout of microbeam and Bragg gratings.

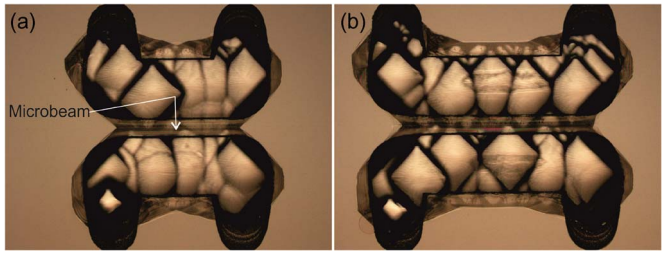

Fig. 5. Microscope images of the microbeams following KOH wet etch. (a) 1 mm. (b) 1.5 mm. The arrow locates the glass microbeam separated from the underlying silicon floor.

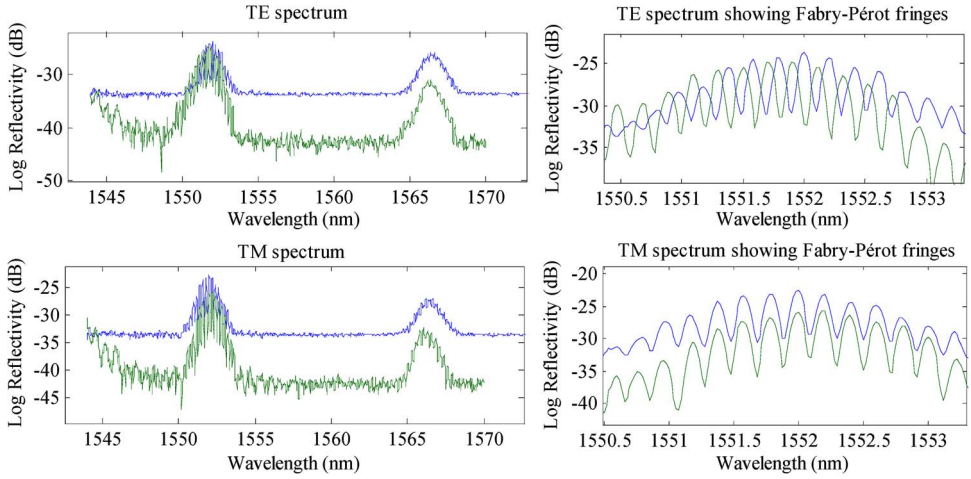

Fig. 6. Comparison of spectra before (blue line) and after etching (green line) for the TE and TM modes.

used as a rough mask for the heating strip. A microscope image following this step is shown in Fig. 7. The reduction in width across the microbeam ensures that the majority of Joule heating will occur in this region. The metallic heater element is separated by 17 microns of cladding glass from the core of the waveguide, thus ensuring that the optical field does not suffer attenuation due to the metal. Using a grating based method [21]. We can estimate that there is negligible additional loss from the microbeam fabrication beyond the ~0.2 dB/cm intrinsic loss of the waveguides themselves.

A scanning electron microscope was used to image the device to confirm that it had been fully undercut. Fig. 8 shows two SEM images for two different lengths of microbeam.

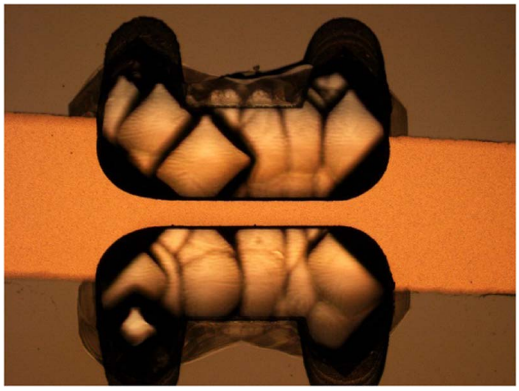

Fig. 7. Optical microscope image of microbeam following the Cr+Au deposition.

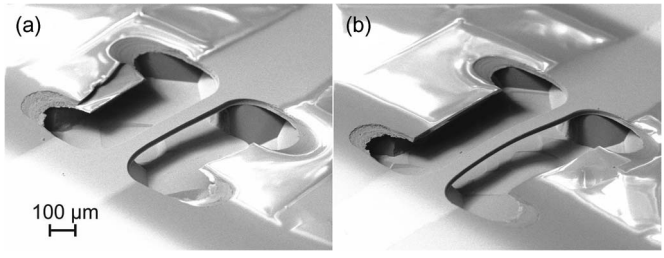

Fig. 8. SEM images showing released microbeams. (a) 1 mm. (b) 1.5 mm.

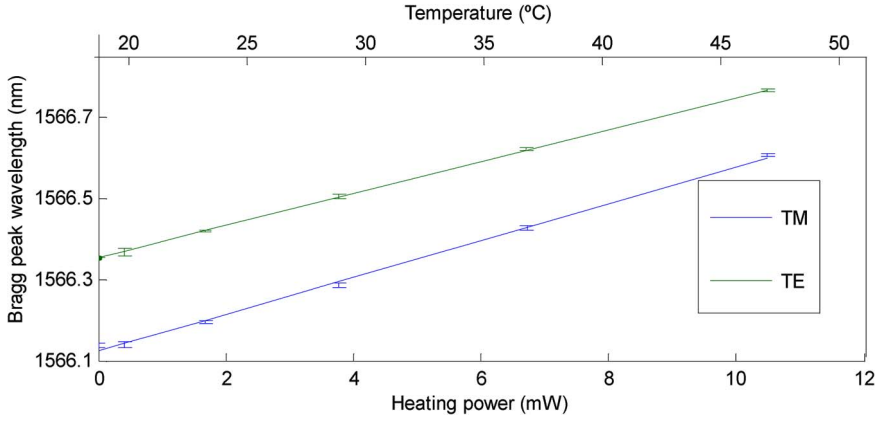

Fig. 9. Shift in central Bragg peak wavelength with electrical heating power. The top axis also shows the temperature reached by the microbeam as measured by a 4-point-probe technique.

4. Characterization

4.1. Thermo-Optical Characterization

With the heating element deposited the tuning of each Bragg grating's reflection wavelength with heating power was studied. An Optical Spectrum Analyzer (OSA) was used to measure the reflection spectrum of the device for a range of heating powers. Gaussian fitting to the Bragg peak allows the peak Bragg wavelength to be plotted as a function of heating power. The optical setup includes a polarizer which allows the TM and TE modes to be studied independently. Fig. 9 shows the shift in central Bragg peak wavelength with electrical heating power. In

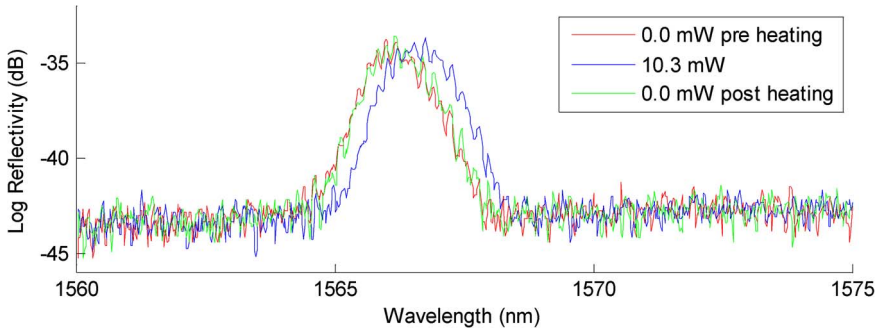

Fig. 10. Spectra showing Bragg peak during tuning. The spectrum at maximum heating is shown in blue and indicates that the spectral shape and height are preserved during tuning.

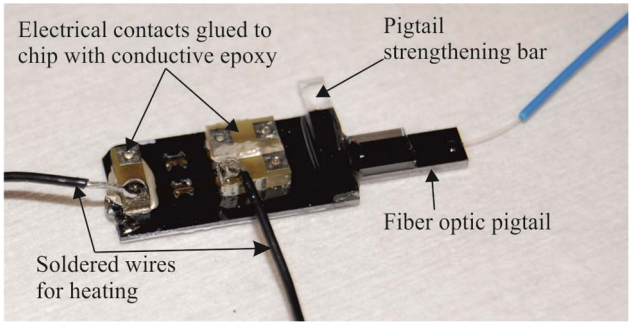

Fig. 11. Completed device showing location of microbeam, fiber optic pigtail, and electrical contacts.

addition, the average temperature of the microbeam during tuning is shown. This was measured using a 4-point-probe method which will be described later in the report.

It can be seen that the tuning efficiency is slightly higher for TM 45 $\pm$ 2 pm/mW versus 39 $\pm$ 1 pm/mW for TE. This is believed to be due to the inherent in-plane fabrication stress in the silica which means the material behaves anisotropically when heated. The Bragg peak shift is linear in power for both modes. For a tunable reflector device it is desirable that the spectral shape of the Bragg peak is maintained during tuning. Fig. 10 shows that this is the case over the tuning range studied. The fringes in Fig. 10 result from interference between the Bragg grating response and imperfectly terminated end-facets and this is confirmed by the period of the fringes. The gratings in this device were Gaussian apodized but can, in principle, be designed to offer more advanced functionality as commonly used in laser written Bragg gratings [22].

Fig. 11 shows a photograph of the completed device which has a footprint of 10 mm $\times$ 20 mm and a height of 3 mm.

A four-point probe measurement was conducted to find the temperature reached by the microbeam. During tuning the current supplied to the heating element was measured using an Agilent U1253A multimeter and the voltage drop across the element was measured using a Keithley 2100 multimeter. From these data the I-V relationship for the thin film heating element was established. The temperature dependent coefficient of resistance was determined by bulk heating of the device and performing the 4-point probe measurement at low current to reduce extra heating. The experimentally determined temperature coefficient of resistance was determined to be 0.00230(6) $^{\circ}C^{-1}$. It has previously been reported that in thin metallic gold films this value is lower than for the bulk material [23]. The data in Fig. 9 includes the inferred temperatures reached during Bragg peak tuning. It can be seen an average temperature of 47 $^{\circ}$C is reached at the maximum of the tuning. The tuning efficiency of this device is approximately a factor of 90 better than a thermally tunable Bragg grating in a bulk silica device [15]. The limiting factor to

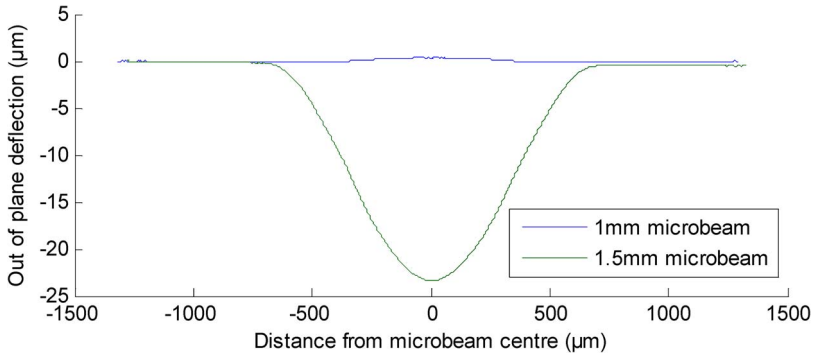

Fig. 12. Deflection of microbeams following etch release. The shorter microbeam shows slight out-of-plane deflection, whilst the longer 1.5 mm microbeam has undergone buckling.

the tuning range is expected to be either the erasure of the Bragg grating at high temperatures or the additional mechanical stress during tuning.

5. Thermo-Mechanical Characterization

Following the optical characterization the mechanical behavior of the microbeam during tuning/heating was also investigated. Localized heating causes a thermal deformation of the microbeam. The microbeams were characterized mechanically using a Zemetrics Zescope optical profiler. The Zescope records 3-D surface plots from which line slices of height can extracted. Fig. 12 shows the measured microbeam profiles without any applied heating. The sign convention is with positive deflection being out of the plane of the device.

It can be seen that for the 1 mm long microbeam there is a small positive deflection of 0.4 μm. The 1.5 mm microbeam has deflected downwards by 23.3 μm. This strongly suggests only the 1.5 mm microbeam has buckled. The direction of buckling is downwards, towards the silicon substrate. This direction offers greater strain relief to the thermal oxide underclad, which has higher initial compressive stress than the FHD overclad. An upwardly buckled microbeam may also be locally stable and further work would be possible to determine the repeatability and the effect of etching conditions on the buckling direction. The effect of heating on the deflection was also investigated for both the buckled and unbuckled microbeams. Fig. 13 shows how the center points of the microbeams moved under increasing heating.

This data shows that the buckled microbeam deflects further out of the plane for a given heating power than the unbuckled microbeam. This is expected as the buckled microbeam is less constrained to deflect out of plane. The direction of the heating induced deflections follow the direction of initial movement following etch release.

6. Response Time

The increased energy efficiency of this device comes at penalty of a slower time response. The response time to a switch-on voltage of 0.5 V was measured using an optical setup consisting of a tunable laser tuned to wavelength which coincides with a spectrally narrow Fabry–Pérot fringe. From the tuning efficiency results obtained this is equivalent to a peak shift of 0.43 nm for the TM mode.

The tunable laser was tuned to 1552.13 nm which was found to be between a maxima and minima on the Fabry–Pérot pattern. When heated the optical path length of the microbeam increased changing the cavity length of the Fabry–Pérot cavity. The heating power used only increased the cavity length by a fraction of one wavelength and so the response from the photodiode was approximated to be linear with heating. For the switch-on, a 1/e time of 44 $\pm$ 3 ms was obtained, and for the switch-off, 50 $\pm$ 1 ms was measured. This is a factor of $\sim$50 slower than the tuning response times reported for Bragg gratings in bulk silica

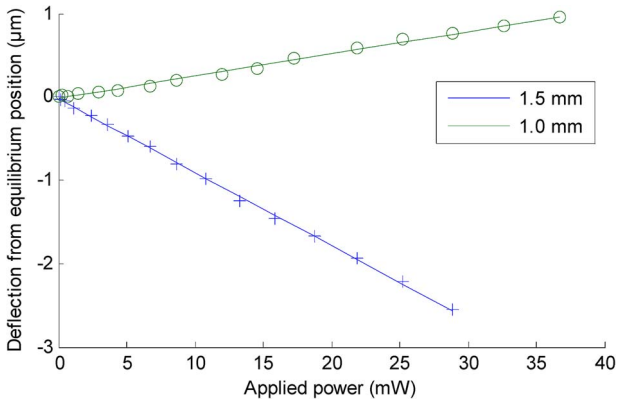

Fig. 13. Effect of heating on microbeam deflection. The buckled microbeam shows greater out-of-plane growth for the same applied heating power as the unbuckled microbeam.

substrates and confirms that the trade-off for the device is between greater power efficiency and response time [15]. For applications in data-center switching or dispersion compensation our response times are sufficient, while for other applications, devices with greater power consumption and high switching speeds may be preferable.

7. Conclusion

A silica-on-silicon device that allows tuning of a Gaussian apodized Bragg grating has been demonstrated. Tuning efficiency is enhanced by incorporating the Bragg grating into a microbeam which gives greater thermal isolation and acts as a smaller thermal mass. Tuning efficiency of 45 pm/mW for the TM mode and 39 pm/mW for the TE mode has been achieved which is a factor of 90 better than for a bulk silica device. The device could find applications where highly efficient tuning and low thermal cross-talk is required. Tuning has been shown over a range of 0.4 nm corresponding to 50 GHz which is appropriate for telecommunication DWDM applications. The 1.5 mm long microbeam buckled following the etch release step. This feature has the potential to create a bistable switch that would not require continuous power supply to tune between two states.

References

[1] H. Guckel, T. Randazzo, and D. W. Burns, "A simple technique for the determination of mechanical strain in thin films with applications to polysilicon," *J. Appl. Phys.*, vol. 57, no. 5, pp. 1671–1675, Nov. 1984.
[2] T. Lisec, S. Hoerschelmann, H. J. Quenzer, B. Wagner, and W. Benecke, "Thermally driven microvalve with buckling behaviour for pneumatic applications," in *Proc. IEEE Workshop Micro Electro Mech. Syst.*, 1994, pp. 13–17.
[3] D. J. Joe *et al.,* "Stress-based resonant volatile gas microsensor operated near the critically buckled state," *J. Appl. Phys.*, vol. 111, no. 10, May 2012, Art. ID. 104517.
[4] A. Sugita, "Bridge-suspended silica-waveguide thermo-optic phase shifter and its application to Mach-Zehnder type optical switch," in *Proc. Int. Conf. Integr. Opt. Fiber Commun.*, 1990, pp. 105–109.
[5] C. R. Raum, R. N. Tait, and R. C. Gauthier, "Fabrication and characterization of a thermo-mechanically tunable grating-assisted suspended waveguide filter," in *Proc. SPIE*, 2008, vol. 6898, pp. 1–9.
[6] B. Calkins *et al.,* "High quantum-efficiency photon-number-resolving detector for photonic on-chip information processing," *Opt Exp.*, vol. 21, no. 19, pp. 22 657–22 670, Sep. 2013.
[7] A. Iocco *et al.,* "Bragg grating fast tunable filter for wavelength division multiplexing," *J Lightw. Technol.*, vol. 17, no. 7, pp. 1217–1221, Jul. 1999.
[8] B. J. Eggleton *et al.,* "Integrated tunable fiber gratings for dispersion management in high-bit rate systems," *J Lightw. Technol.*, vol. 18, no. 10, pp. 1418–1432, Oct. 2000.
[9] L. G. Carpenter, C. Holmes, H. L. Rogers, P. G. R. Smith, and J. C. Gates, "Integrated tunable fiber gratings for dispersion management in high-bit rate systems," *Opt. Exp.*, vol. 18, no. 22, pp. 23 296–23 301, Oct. 2010.
[10] C. Holmes, L. G. Carpenter, J. C. Gates, and P. G. R. Smith, "Miniaturization of Bragg-multiplexed membrane transducers," *J Micromech. Microeng.*, vol. 22, no. 2, Feb. 2012, Art. ID. 025017.
[11] B. J. Metcalf *et al.,* "Quantum teleportation on a photonic chip," *Nature Photon.*, vol. 8, no. 10, pp. 770–774, Sep. 2014.

[12] S. Donati, L. Barbieri, and G. Martini, "Piezoelectric actuation of silica-on-silicon waveguide devices," *IEEE Photon. Technol. Lett.*, vol. 10, no. 10, pp. 1428–1430, Oct. 1998.
[13] F. R. Mahamd Adikan *et al.,* "Demonstration of 100 GHz electrically tunable liquid-crystal Bragg gratings for application in dynamic optical networks," *Opt. Lett.*, vol. 32, no. 11, pp. 1542–1544, Jun. 2007.
[14] J. H. Wray and J. T. Neu, "Refractive index of several glasses as a function of wavelength and temperature," *J. Opt. Soc. Amer.*, vol. 59, no. 6, pp. 774–776, Jun. 1969.
[15] C. Holmes, D. O. Kundys, C. B. E Gates, J. C. Gawith, and P. G. R. Smith, "150 GHz of thermo-optic tuning in direct UV written silica-on-silicon planar Bragg grating," *Electron. Lett.*, vol. 45, no. 18, pp. 954–955, Aug. 2009.
[16] P. C. Humphreys *et al.,* "Strain-optic active control for quantum integrated photonics," *Opt Exp.*, vol. 22, no. 18, pp. 21 719–21 726, Sep. 2014.
[17] B. G. Aitken and R. E. Youngman, "Borophosphosilicate glasses: Properties and structure," *Phys. Chem. Glasses*, vol. 47, no. 4, pp. 381–387, Aug. 2006.
[18] J. M. Gere and S. P. Timoshenko, *Mechanics of Materials*, 4th ed. Cheltenham, U.K.: Stanley Thornes, 1999.
[19] L. G. Carpenter *et al.,* "Nanoscale roughness micromilled silica evanescent refractometer," *Opt. Exp.*, vol. 23, no. 2, pp. 1005–1014, Jan. 2015.
[20] G. D. Emmerson *et al.,* "Fabrication of directly UV-written channel waveguides with simultaneously defined integral Bragg gratings," *Electron. Lett.*, vol. 38, no. 24, pp. 1531–1532, Nov. 2002.
[21] H. L. Rogers, S. Ambran, C. Holmes, P. G. R. Smith, and J. C. Gates, "In situ loss measurement of direct UV-written waveguides using integrated Bragg gratings," *Opt Lett.*, vol. 35, no. 17, pp. 2849–2851, Sep. 2010.
[22] R. Kashyap, *Fiber Bragg Gratings*. San Diego, CA, USA: Academic, 1999.
[23] F. Avilés, O. Ceh, and A. I. Oliva, "Physical properties of Au and Al thin films measured by resistive heating," *Surface Rev. Lett.*, vol. 12, no. 1, pp. 101–106, Feb. 2005.